GEOPHYSICS

Synchronizing volcanic, sedimentary, and ice core records of Earth's last magnetic polarity reversal

Brad S. Singer[1]*, Brian R. Jicha[1], Nobutatsu Mochizuki[2†], Robert S. Coe[3]

Reversal of Earth's magnetic field polarity every 10^5 to 10^6 years is among the most far-reaching, yet enigmatic, geophysical phenomena. The short duration of reversals make precise temporal records of past magnetic field behavior paramount to understanding the processes that produce them. We correlate new $^{40}Ar/^{39}Ar$ dates from transitionally magnetized lava flows to astronomically dated sediment and ice records to map the evolution of Earth's last reversal. The final 180° polarity reversal at ~773 ka culminates a complex process beginning at ~795 ka with weakening of the field, succeeded by increased field intensity manifested in sediments and ice, and then by an excursion and weakening of intensity at ~784 ka that heralds a >10 ka period wherein sediments record highly variable directions. The 22 ka evolution of this reversal suggested by our findings is mirrored by a numerical geodynamo simulation that may capture much of the naturally observed reversal process.

INTRODUCTION

Reversals of Earth's magnetic field are global manifestations of instability that develops within the outer core geodynamo. To understand processes in the core that propel reversals, and to predict how the Earth system would respond to a future reversal, it is critical to map out a detailed description of the global geomagnetic field that occurs during the transition between long-lived, relatively stable, polarity states (*1*–*3*). Yet, despite decades of study, the geometric structure, timing, and duration of reversals remain enigmatic, principally because they are short-lived phenomena and thus high-resolution recordings are sparse and difficult to date. The Matuyama-Brunhes (M-B) reversal is the most studied because it has been identified in dozens of marine sediment cores [e.g., (*2*, *4*–*11*)], exposed sedimentary successions [e.g., (*12*, *13*)], and a few lava flow sequences (*14*–*17*). Moreover, the M-B reversal is an important global temporal marker (*18*) key to defining the Lower-Middle Pleistocene boundary and, thus, to correlating among records associated with the profound shift of global climate dynamics into a state dominated by 100 ka (ka = thousand years) oscillations (*19*, *20*).

Although the vast majority of M-B transition records come from marine sediment cores, sedimentary archives can be degraded with respect to magnetic fidelity and temporal resolution; thus, inferences about the reversing field are controversial (*1*, *2*, *21*). Key issues that may complicate sedimentary records include depositional processes, low deposition rates (*22*, *23*), weak magnetization, and, in some cases, remagnetization [e.g., (*24*)]. When compared to volcanic records, the impact of deposition rates lower than 10 cm/ka and increased magnetic lock-in depth results in smoothing or "smearing" of geomagnetic field directions (*1*, *2*) and thus loss of geometric and temporal resolution. Moreover, even at sediment deposition rates of 10 cm/ka, bioturbation and magnetic lock-in processes can convolute magnetic remanence signals and decrease the temporal resolution to 1 to 2 ka or less. These effects may be amplified owing to the response of magnetometers used to measure U-channels from long sediment cores that integrate signals and lead to smoothing of records over several centimeters of core (*1*, *25*).

On the other hand, the thermoremanent magnetization of lava flows can provide well-understood "spot" recordings of the magnetic field geometry as virtual geomagnetic poles (VGPs), as well as intensity, as they cool (*3*, *14*, *15*, *26*). Sequences of flows are among the best materials also because successive lavas can provide temporal records of paleointensity together with paleodirection, both tied to $^{40}Ar/^{39}Ar$ dating [e.g., (*16*, *27*)]. An examination of lava flow records led to the bold proposal by Valet *et al.* (*26*) that all reversals share a common three-phase evolution including a precursor, a 180° reversal of the dipole field, and a rebound in which weak nondipole fields emerge during the first and third phases. We examine this proposal in light of our new, more accurate timeline for lava flows associated with the M-B reversal.

We present new $^{40}Ar/^{39}Ar$ dates within six volcanic sections that record transitional geomagnetic field directions and, in some cases, intensity variations, associated with the M-B reversal. The VGPs of these lava flow sequences are correlated to several high–deposition rate sediment recordings of paleomagnetic field direction and intensity for which astrochronologic age models have been derived. Cosmogenic ^{10}Be proxy records of paleomagnetic field intensity in Antarctic ice and Indian Ocean sediment are also correlated to the volcanic record. The integration of $^{40}Ar/^{39}Ar$-dated lava, sediment, and ice recordings reveals extraordinary complexity in the evolution of the geomagnetic field during a ≥22 ka period leading up to and including the final M-B reversal. Moreover, during this period, lava flow VGPs define paths and clusters over Australasia, North America, and Southern South America. The observed behavior is consistent with the hypothesis that demise of the axial dipole field allows a weak non-axial dipole (NAD; the residual field left after subtracting out the axial dipole) field to emerge from the shallow core (*28*) repeatedly during the waning stages of the Matuyama Chron.

Lava flow sequences thought to record fragmentary pieces of the M-B process are known on the south (*29*) and north (*16*) walls of Punaruu Valley, Tahiti; in two adjacent superposed sequences on the west wall of Quebrada Turbia, Chile (*30*); in Guadeloupe (*17*); in

[1]Department of Geoscience, University of Wisconsin-Madison, 1215 West Dayton Street, Madison, WI 53706, USA. [2]Priority Organization for Innovation and Excellence, Kumamoto University, Kumamoto 860-8555, Japan. [3]Earth Sciences Department, University of California, Santa Cruz, CA 95064, USA.
*Corresponding author. Email: bsinger@geology.wisc.edu
†Present address: Department of Earth and Environmental Sciences, Kumamoto University, Kumamoto 860-8555, Japan.

Los Tilos canyon, La Palma (*31*); and in the Haleakala "caldera," Maui (Fig. 1) (*14*). We note that the two lava sequences in Chile are superposed on the same wall of the Quebrada Turbia canyon such that the entire section records reverse-transitional-normal polarities with a reversely magnetized lava dated at 816 ka at the base of the QTW (Quebrada Turbia West) 10 section, and 1 km to the north, the top of the entire section is recorded in the QTW 11 sequence that terminates with three normally magnetized lavas (*30*). More than two decades ago, the $^{40}Ar/^{39}Ar$ ages determined from 11 lava flows in the sections at Punaruu South, La Palma, Chile, and Haleakala led to the conclusion that the M-B reversal may have lasted >12 ka (*32*). Subsequent $^{40}Ar/^{39}Ar$ experiments yielded additional ages from these sections (*14*, *30*, *31*) plus the sequence of three R-T-R (reverse-transitional-reverse) lava flows on Guadeloupe (*17*). Singer *et al.* (*15*) integrated the geochronology and paleomagnetic directions of 23 lavas at Punaruu South, Chile, La Palma, and Haleakala to conclude that most of these sequences record geodynamo instability associated with an M-B precursor that occurred ~18 ka before the reversal, which is well recorded only at Haleakala. These $^{40}Ar/^{39}Ar$ ages were determined from large samples (~200 to 450 mg) using single-collector mass spectrometers and gas extraction systems that used resistance furnaces, which had background levels of argon that were relatively high, non-atmospheric in composition, and infrequently measured compared to modern procedures (see the Supplementary Materials) (*18*). Low and frequently measured system blanks and careful monitoring of mass discrimination are paramount to obtaining accurate and precise dates from Pleistocene lava samples in which the majority of ^{40}Ar is not radiogenic (see Methods and the Supplementary Materials). Moreover, a novel calibration of the $^{40}Ar/^{39}Ar$ method against astronomically dated marine sediments yields an age for the widely used Fish Canyon sanidine (FCs) standard of 28.201 ± 0.046 Ma that improved both the accuracy and precision of the method by an order of magnitude (*33*). Yet, recalculating the 23 ages determined by Singer *et al.* (*15*) using this new age of FCs results in a mismatch by 8 ka, or about 1%, between the lavas that record the reversal at Haleakala and the astronomical ages of 773 ± 1 ka determined for the M-B reversal in five North Atlantic sediment cores (*34*) and 773 ka in the Chiba section, Japan (*20*), that is also independently calibrated by a $^{206}Pb/^{238}U$ zircon age of 772.7 ± 7.2 ka for the ByK-E tuff (*13*). We emphasize that, because of the issues noted above regarding how system blank measurements associated with the 23 $^{40}Ar/^{39}Ar$ dates summarized by Singer *et al.* (*15*) limit their accuracy to ~2% relative, it is inappropriate to simply recalculate these using the astronomically calibrated age of the FCs standard as has been done by several researchers (*34*–*36*) (see the Supplementary Materials). To capitalize on the astronomical calibration of FCs (*33*), as well as the exceptionally low blanks and counting statistic advantages of an ion counting multicollector mass spectrometer (*37*, *38*), we obtained new $^{40}Ar/^{39}Ar$ dates from 40 lavas in the six sequences outlined above using the IH MCMS (incremental-heating, multicollector mass spectrometry) approach (see Methods) to improve both the accuracy and precision of the volcanic record of the M-B reversal process.

RESULTS

Lava flow geochronology

Since we are interested in the timing of geodynamo instabilities, we define a state of transitional polarity as having a VGP latitude between 60° and −60°, but note also that VGPs that fall closer to the geographic pole may also record transient reversals or excursions just before the M-B reversal that are best counted as part of the same unstable interval. The $^{40}Ar/^{39}Ar$ experiments typically yield plateau dates with 2σ uncertainties of ±1% (±7 ka) or better (Table 1 and Fig. 2). Of the eight lava flows dated from the composite section in Chile, six have transitional VGPs, four of which have a virtual dipole moment (VDM) below 2×10^{22} Am^2, indicating that the field was also very weak. For reference, the mean VDM during the last 100 ka of the Brunhes Chron is 6.83×10^{22} Am^2, with the lowest value of 2.46×10^{22} Am^2 occurring during the Laschamp excursion (*39*). These six lavas yield $^{40}Ar/^{39}Ar$ ages ranging from 786 ± 5 to 781 ± 6 ka

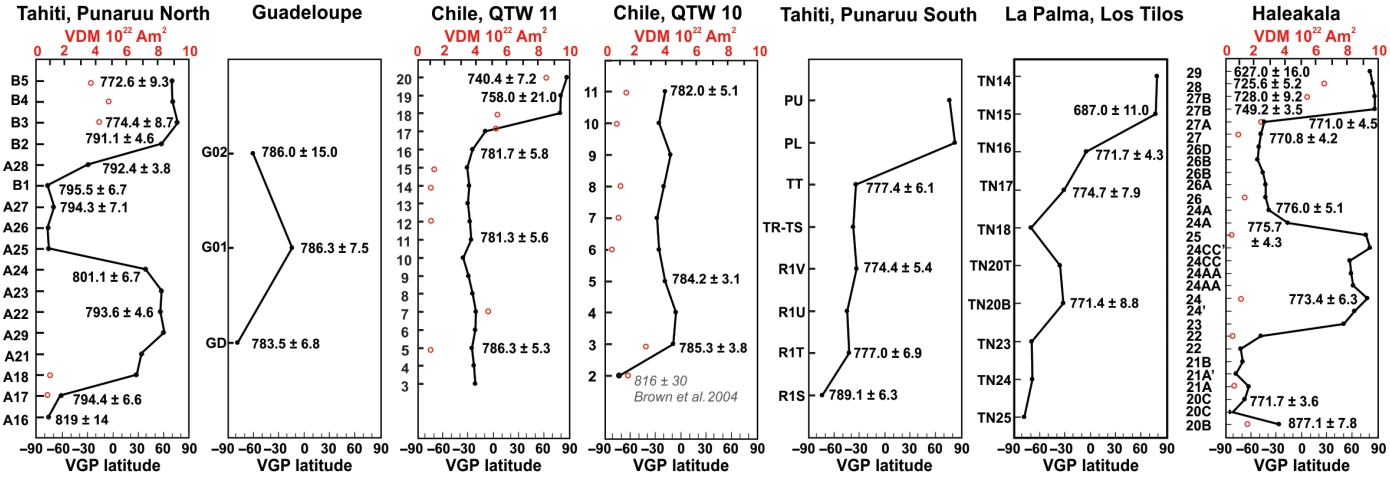

Fig. 1. Lava flow sequences that record transitional geomagnetic field behavior associated with the Matuyama-Brunhes reversal. Vertical axes are the lava flow site numbers from the original studies arranged in order of eruption from oldest at the bottom to youngest on top. VGP lat., virtual geomagnetic pole latitude in degrees. $^{40}Ar/^{39}Ar$ ages (in thousand years) for dated flows are shown with ±2σ analytical uncertainties. The paleomagnetic directional data are from Punaruu South, Tahiti (*29*); Quebrada Turbia West-10 and West-11, Chile (*30*); Los Tilos, La Palma (*31*); Punaruu North, Tahiti (see the Supplementary Materials) (*16*); Guadeloupe (*17*); and Haleakala (*14*). The red open circles are determinations of the virtual dipole moment (VDM) for samples measured in this study from Haleakala (see the Supplementary Materials), Punaruu North [data from (*16*)], and Chile [data from (*27*)].

Table 1. Summary of $^{40}Ar/^{39}Ar$ data from lava flow sites. Ages calculated relative to 1.1864 Ma Alder Creek sanidine standard (*37*). Decay constants are from (*52*). Atmospheric $^{40}Ar/^{36}Ar = 298.56 \pm 0.31$ (*57*). No. of expts, number of experiments performed on each sample. *N*, number of steps included from the total.

Sample	VGP lat. (°)	No. of expts	Total fusion		Isochron				Plateau
			Age (ka) ± 2σ	$^{40}Ar/^{36}Ar_i \pm 2\sigma$	Age (ka) ± 2σ	*N*	^{39}Ar %	MSWD	Age (ka) ± 2 σ
Haleakala									
H-15-29	80.6	1	618 ± 19	300 ± 6	617 ± 66	10 of 11	95.5	0.87	627.0 ± 16.0
H-15-28	84.2	2	734 ± 5	300 ± 4	715 ± 23	23 of 34	75.3	0.98	725.6 ± 5.2
86C529A/27B2	86.5	1	732 ± 8	300 ± 7	717 ± 66	14 of 16	88.7	0.44	727.9 ± 9.2
85M001A/27B	86.5	2	744 ± 3	302 ± 5	740 ± 14	17 of 21	76.5	0.89	749.2 ± 3.5
H-15-27A	−44.2	3	764 ± 5	299 ± 3	767 ± 19	40 of 51	88.1	0.50	771.0 ± 4.5
H-15-27	−47.9	4	752 ± 4	298 ± 3	781 ± 22	46 of 69	76.1	0.67	770.8 ± 4.2
84C436A/25A	−38.2	4	766 ± 3	298 ± 3	778 ± 25	59 of 77	79.4	0.86	773.9 ± 3.5
H-15-24A	−16.7	1	754 ± 3	299 ± 6	776 ± 13	9 of 15	82.8	0.29	775.7 ± 4.3
H-15-24	62.0	3	756 ± 7	297 ± 3	772 ± 25	33 of 58	77.2	0.92	773.4 ± 6.3
H-15-21	−67.5	6	753 ± 4	298 ± 3	775 ± 20	59 of 80	85.0	0.41	771.7 ± 3.6
Quebrada Turbia, Chile									
QTW11-20	87.4	1	711 ± 8	295 ± 9	754 ± 31	9 of 14	77.8	0.93	740.4 ± 7.2
QTW11-19	80.2	1	742 ± 19	297 ± 6	775 ± 96	6 of 9	84.1	0.91	758.0 ± 21.0
QTW11-16	−24.8	1	766 ± 5	299 ± 7	780 ± 19	10 of 16	78.4	0.63	781.7 ± 5.8
QTW11-11	−26.1	1	754 ± 6	299 ± 7	770 ± 28	11 of 17	78.9	0.43	781.4 ± 5.6
QTW11-5	−25.7	1	775 ± 4	299 ± 10	787 ± 24	10 of 16	83.6	1.60	786.3 ± 5.3
QTW11-3	−21.8	1	766 ± 7	296 ± 6	783 ± 28	11 of 18	78.4	0.79	785.0 ± 6.6
QTW10-10	−25.6	1	779 ± 4	296 ± 6	787 ± 13	10 of 12	91.5	0.77	782.0 ± 5.1
QTW10-5	−18.6	1	779 ± 2	297 ± 9	776 ± 17	8 of 21	56.7	1.13	784.2 ± 3.1
QTW10-3	−8.9	1	782 ± 3	296 ± 8	787 ± 7	12 of 14	95.8	0.85	785.3 ± 3.8
Guadeloupe									
GA0207B	−61.0	1	713 ± 16	298 ± 6	784 ± 63	8 of 14	67.8	0.29	786.0 ± 15.0
GA010B	−14.4	1	746 ± 8	298 ± 14	778 ± 42	8 of 13	80.1	0.64	786.3 ± 7.5
GD0103B	−79.0	1	766 ± 7	299 ± 4	772 ± 16	9 of 15	64.9	0.83	783.5 ± 6.8
Tahiti: Punaruu South									
TT	−34.0	1	743 ± 6	296 ± 10	778 ± 41	8 of 17	63.2	0.60	777.4 ± 6.1
R1V	−33.1	2	768 ± 8	300 ± 4	766 ± 15	15 of 30	71.6	0.73	774.4 ± 5.4
R1T	−41.9	1	741 ± 6	294 ± 8	791 ± 46	9 of 18	57.5	0.56	777.0 ± 6.9
R1S	−73.5	1	755 ± 8	301 ± 7	772 ± 24	9 of 16	77.7	0.75	789.1 ± 6.2
Tahiti: Punaruu North									
TM28	74.6	1	713 ± 9	299 ± 8	761 ± 40	8 of 13	63.0	0.41	772.6 ± 9.3
TM30	81.5	1	734 ± 10	300 ± 4	765 ± 26	11 of 17	84.1	0.69	774.4 ± 8.7
TM31	62.5	2	771 ± 5	297 ± 3	785 ± 13	17 of 29	78.1	0.65	791.1 ± 4.6
TM32	−71.9	2	745 ± 9	298 ± 5	789 ± 34	19 of 37	80.4	0.81	795.5 ± 6.7
TM24	−24.5	2	769 ± 4	296 ± 4	795 ± 13	18 of 29	79.3	1.07	792.4 ± 3.8
TM23	46.6	1	775 ± 9	298 ± 3	788 ± 15	10 of 15	81.6	0.56	794.3 ± 7.1
TM27	43.5	1	792 ± 7	294 ± 19	796 ± 26	7 of 12	67.9	0.49	801.1 ± 6.7
TM20-5	61.3	2	772 ± 6	298 ± 3	785 ± 15	21 of 35	84.3	0.65	793.6 ± 4.6
TM18	56.5	1	752 ± 8	297 ± 12	790 ± 44	6 of 14	62.1	0.47	794.4 ± 6.7
TM13	−70.0	1	689 ± 10	298 ± 8	821 ± 46	6 of 13	56.1	0.34	819.0 ± 13.0

continued to next page

Sample	VGP lat. (°)	No. of expts	Total fusion Age (ka) ± 2σ	$^{40}Ar/^{36}Ar_i \pm 2\sigma$	Isochron Age (ka) ± 2σ	*N*	^{39}Ar %	MSWD	Plateau Age (ka) ± 2 σ
La Palma									
TN15	76.7	1	681 ± 13	299 ± 3	675 ± 36	20 of 22	94.1	0.47	687.0 ± 11.0
TN16	−5.4	2	765 ± 5	298 ± 1	766 ± 12	43 of 46	93.4	0.85	771.7 ± 4.3
TN17	−31.1	1	762 ± 9	299 ± 3	762 ± 29	15 of 19	92.3	0.76	774.3 ± 7.9
TN20	−31.6	2	739 ± 6	296 ± 6	785 ± 29	16 of 34	70.7	0.97	774.8 ± 5.3

(Figs. 1 and 2). Two overlying flows that have normal polarity VGPs and VDMs > 4×10^{22} Am^2 are dated at 758 ± 21 and 740 ± 7 ka (Table 1 and Figure 1). The ages of the six flows with transitional VGPs are indistinguishable from one another at the 95% confidence level and yield an inverse-variance weighted mean of 784 ± 2 ka with mean square weighted deviation (MSWD) of 0.13. We infer that the 24 transitionally and weakly magnetized lava flows in the composite section in Chile record a brief period of magnetic field instability centered on 784 ± 2 ka (Fig. 1). In the Guadeloupe section, a single transitionally magnetized lava flow is sandwiched between flows with reverse magnetizations (Fig. 1). These three lavas yield $^{40}Ar/^{39}Ar$ ages of 784 ± 7, 786 ± 8, and 786 ± 15 ka that are indistinguishable from one another. The weighted mean age of 785 ± 5 ka (MSWD = 0.02) constrains the timing of the transitional magnetization recorded in this sequence and is thus temporally indistinguishable from the transitional recording in Chile.

From the Punaruu South section, Tahiti, a reversely magnetized lava yields a $^{40}Ar/^{39}Ar$ age of 789 ± 6 ka, whereas three of five transitionally magnetized lavas that overlie it yield ages of 777 ± 7, 774 ± 5, and 777 ± 6 ka that are indistinguishable from one another (Table 1 and Fig. 1). The weighted mean of 776 ± 3 ka (MSWD = 0.10) gives the age for the recording of transitional field behavior captured by these five lava flows and is distinctly younger than the recordings in Chile and Guadeloupe.

For the Punaruu North section, we have slightly modified the stratigraphic relations and the sequence of paleomagnetic data originally proposed by Mochizuki *et al.* (*16*) (see the Supplementary Materials). This section records an excursion from reversed to nearly normal polarity recorded in seven successive lava flows, followed by a shift back to reversed polarity recorded in five successive flows that, in turn, is followed by one transitional flow and four flows that record normal polarity (Fig. 1). Paleointensity determinations suggest that the geomagnetic field was weak, with the VDM less than 1×10^{22} Am^2 at the onset of these reversals (Fig. 1) (*16*). We have obtained $^{40}Ar/^{39}Ar$ ages of 794 ± 7, 794 ± 5, 801 ± 7, 794 ± 7, 795 ± 7, 796 ± 7, and 791 ± 5 ka from seven lavas in the part of this section that records the reverse-transitional-reverse-normal behavior (Table 1 and Figs. 1 and 2) that are indistinguishable from one another, given the uncertainties. In addition, we obtained a $^{40}Ar/^{39}Ar$ age of 819 ± 13 ka for a reversely magnetized lava below this part of the section and ages of 774 ± 9 and 773 ± 9 ka for two normally magnetized lavas at the top of this section (Fig. 1). $^{40}Ar/^{39}Ar$ ages for 13 flows in the Punaruu North section, including 9 of the flows we have dated, are reported in (*36*). With only one exception—where our age of 774 ± 9 ka for normally magnetized flow B3 is younger than the age of 792 ± 5 ka determined by Balbas *et al.* (*36*)—the results from the two laboratories are indistinguishable considering the analytical uncertainties (fig. S7). We note that the higher paleointensities of the normally magnetized lavas we have dated at 774 ± 9 and 773 ± 9 ka are consistent with eruption of lavas comprising this part of the section during the earliest Brunhes Chron and thus are inconsistent with the age of 792 ka determined by Balbas *et al.* (*36*) for flow B3 (Fig. 1 and fig. S7). At face value, our age determinations and those of Balbas *et al.* (*36*) for the section comprising the three equator-crossing shifts in the VGP direction (flows A22 through B2; Fig. 1 and fig. S4.1) suggest that these could conceivably have occurred over a span of 10 to 14 ka just preceding 791 ka. However, the weighted mean of our ages and those of Balbas *et al.* (*36*) are 794 ± 2 ka (MSWD = 0.30) and 797 ± 1 ka (MSWD = 1.60), respectively, opening the possibility that these excursions could have occurred over a period as short as 1 to 2 ka. Reconciling the ages with the directional records, we favor the latter interpretation and conclude that the Punaruu North section records a brief period of geodynamo instability that occurred around 795 ka, which ended well before the period of instability recorded in Chile and Guadeloupe at 784 ka.

Three of six lavas in the Los Tilos, La Palma, section that record a transition from reverse to normal polarity yield $^{40}Ar/^{39}Ar$ ages of 771 ± 9, 775 ± 8, and 772 ± 4 ka (e.g., Fig. 2) that are indistinguishable from one another and give a weighted mean age of 773 ± 3 ka (MSWD = 0.11). An overlying normally magnetized flow yields an age of 687 ± 11 ka (Table 1 and Fig. 1). The Haleakala lava flow section comprises 24 flow sites that record a sequence of shifts from reversed, to normal, to transitional VGPs before a hiatus above which younger, normally magnetized, lavas crop out (Fig. 1). New paleointensity determinations (see Methods) reveal a weak magnetic field with VDMs between 0.46×10^{22} and 2.34×10^{22} Am^2 measured in seven of the transitional lavas (Fig. 1 and tables S2 and S3). Six of the lavas recording the complex transitional VGP behavior yield ages of 772 ± 4, 773 ± 6, 776 ± 4, 774 ± 4, 771 ± 4, and 771 ± 5 ka (Table 1 and Fig. 2) that are indistinguishable from one another and give a weighted mean of 773 ± 2 ka (MSWD = 0.22) that is identical to the mean age of the transition recorded at La Palma.

DISCUSSION

Integration of volcanic, sedimentary, and ice core records

We examined the new $^{40}Ar/^{39}Ar$ age determinations statistically using a probability distribution function (*40*) that takes into account the uncertainties on each dated lava flow (fig. S8). From this analysis, we infer that the lava flow sections record at least three temporally distinctive periods of geodynamo instability that produced transitional,

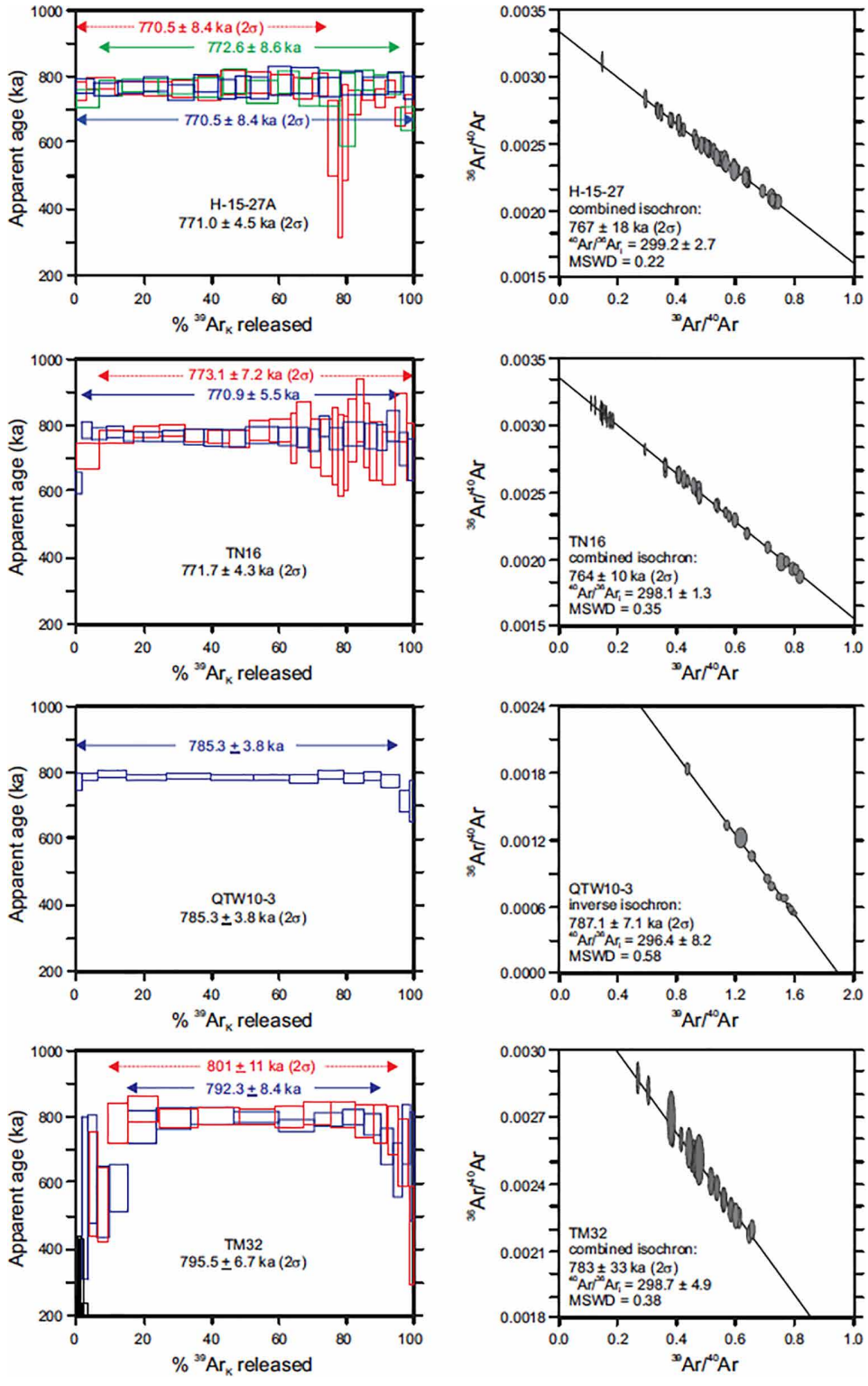

Fig. 2. Age spectra and isochrons from four representative M-B lava samples in Table 1. Samples from bottom to top are from Punaruu North, Chile, La Palma, and Haleakala, respectively.

nondipolar, and weak magnetic fields at around 795 ka (Punaruu North), 784 ka (Chile and Guadeloupe), and 773 ka (Haleakala, La Palma, and Punaruu South; Figs. 3, A and C). To explore beyond these three fragmentary, and likely incomplete, lava recordings of geodynamo instability and build a more continuous map of geomagnetic field behavior during the ≥22 ka period spanned by these lavas, VGP data from several of the highest–deposition rate, and therefore highest-resolution, marine sediment records (Table 2) for

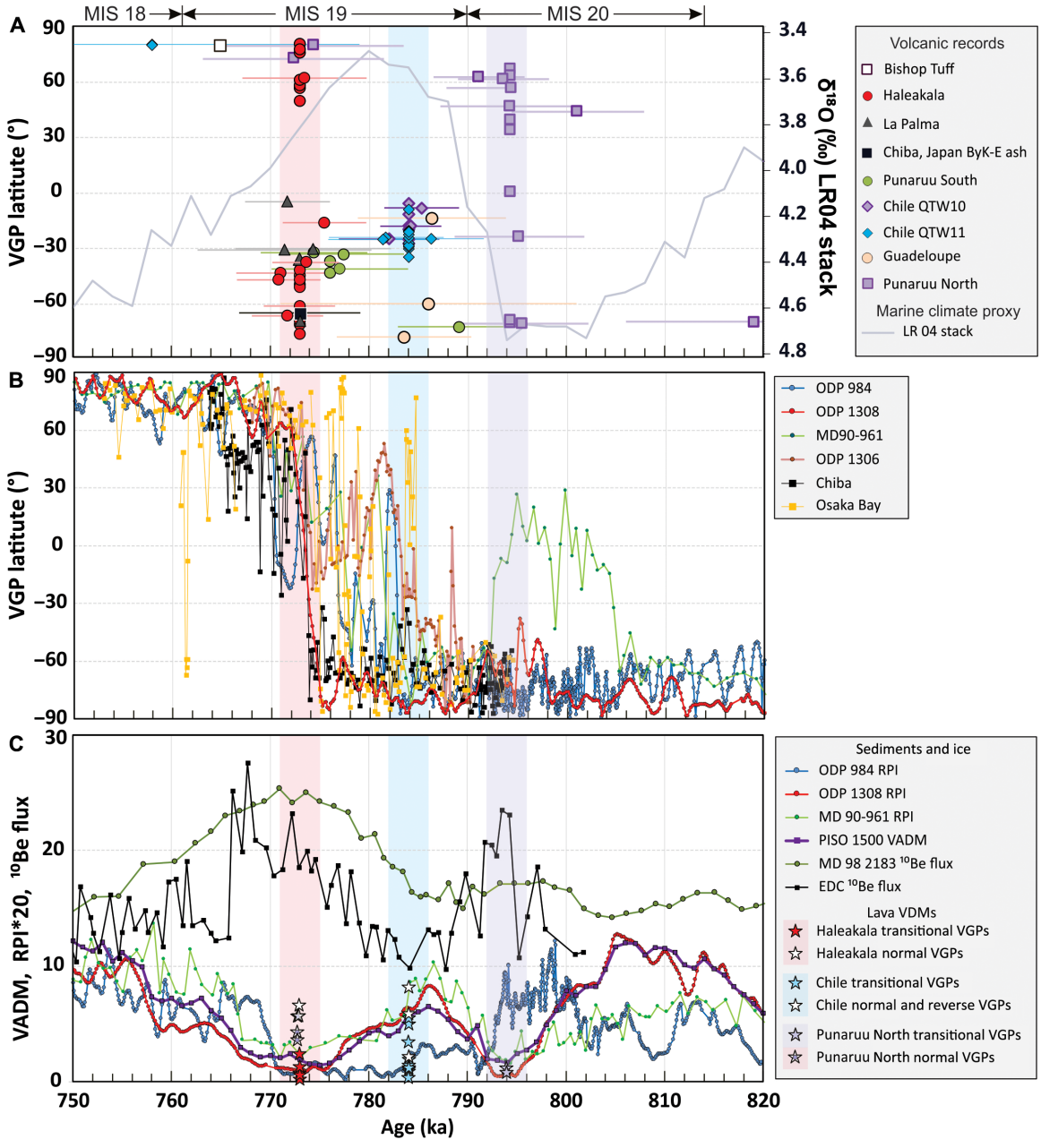

Fig. 3. Correlation of volcanic, sedimentary, and ice core records of geomagnetic field behavior associated with the Matuyama-Brunhes reversal. (**A**) VGPs from dated lavas in each of the seven sections of Fig. 1 are shown with 2σ age uncertainties. The VGPs of undated flows that crop out between dated flows are plotted using the weighted mean age calculated for transitional lavas in each section and are shown without age uncertainty. The purple, blue, and pink vertical bands are the weighted mean ages of lavas in Punaruu North, Chile, and Guadeloupe combined, and Punaruu South, La Palma, and Haleakala combined, respectively, as discussed in the text. (**B**) High–deposition rate marine sediment records of VGP evolution, each placed on its independent astronomical age model (data sources in Table 2) that is not tied to an M-B reversal age. (**C**) Paleointensity proxy records spanning the M-B reversal. Plotted are relative paleointensity (RPI) records (×20) for ODP 984, ODP 1308, and MD90-961 sediment cores; the virtual axial dipole moment (VADM; units of 10^{22} Am^2) for the PISO 1500 stack of 13 marine records; and ^{10}Be flux records [10^4 atoms/g/cm^2 for the Epica Dome (EDC) Antarctic ice core; authigenic decay-corrected ^{10}Be × 10^8 atoms/g for the MD98-2183 marine sediment core; data sources in Table 2)]. Lava VDMs are from this study (table S2) and (*16*, *27*). Note that for gauging paleointensity only, the unfilled stars for normally and reversely magnetized lavas are shown at the same age as the weighted mean age of the associated transitional lavas; see Fig. 1 for ages of these flows.

which astrochronologic age models are available are correlated to the lava flow record (Figs. 3, A and B). Where available from these sedimentary records, as well as the Antarctic ice core record, we also correlate the volcanic record to relative paleointensity or cosmogenic ^{10}Be proxies for paleointensity (Fig. 3C).

Although most sediment records considered here show only limited secular variation of the magnetic field between 820 and 790 ka, the MD90-961 and ODP 1308 cores exhibit excursions correlative to those recorded by lavas at ~795 ka at Punaruu North during the latter third of marine isotope stage (MIS) 20 (Fig. 3, A and B). The sediment

Table 2. Summary of high-resolution sedimentary and ice core records of the M-B reversal.

Site	Site location	Latitude	Longitude	Material	Accumulation rate	Age model	References
ODP site 984	N. Atlantic Ocean, Bjorn Drift	60.4	−23.6	Sediment core	9 cm/ka	Orbitally tuned O-isotope	(*34*, *59*)
ODP site 1308	N. Atlantic Ocean/DSDP site 609	49.9	−24.2	Sediment core	16–18 cm/ka	Orbitally tuned O-isotope	(*34*, *60*)
ODP site 1306	N. Atlantic Ocean, Eirik Drift	58.2	−45.6	Sediment core	15 cm/ka	Orbitally tuned O-isotope/ tandem with RPI	(*2*, *61*)
MD site 90-961	Indian Ocean	5.1	73.8	Sediment core	5 cm/ka	Orbitally tuned O-isotope	(*9*)
Osaka Bay	Osaka Bay, Japan	34.7	135.2	Sediment core	60 cm/ka	Orbitally tuned diatom record of sea level change	(*10*, *11*, *62*)
Chiba	Boso peninsula, Japan	35.3	140.14	Outcrop	63 cm/ka	O-isotope benthic forams correlated to ODP 1123	(*12*, *13*, *20*)
PISO 1500	Composite paleointensity stack			13 sediment cores		O-isotope–coupled correlation to RPI records	(*63*)
MD site 97-2143	Philippine Sea, ^{10}Be paleointensity proxy	15.87	124.7	Sediment core	1.4 cm/ka	Orbitally tuned O-isotope	(*42*)
Epica Dome C	Antarctica, ^{10}Be paleointensity proxy	−75.1	123.3	Ice core		O-isotopes in ice, with tie points orbitally tuned	(*13*, *20*, *44*, *45*)

records generally exhibit only secular variation (except a very brief excursion at ODP 1306) between 790 and 785 ka, during which time a lava flow from Punaruu South records a reversed magnetic field. Sediments at ODP 1306, ODP 984, Chiba, and Osaka Bay record transitional fields with high northern latitude VGPs between 785 and 782 ka that correlate with the weak, intermediate field recorded in the lavas at Chile and Guadeloupe. Between 780 and 770 ka, most of the sediment records contain VGPs that fall well into the Northern Hemisphere (Fig. 3B). The Chiba section, Japan, that was deposited at 63 cm/ka is an exception in that it records limited directional variability about a mean reversed direction, including deposition of the 772.7 ± 7.2 ka ByK-E rhyolitic ash bed in reversely magnetized sediment immediately before the M-B polarity reversal (*12*, *13*, *20*).

We infer that the period of time beginning at ~784 ka represents the onset phase of the M-B polarity reversal featuring the beginning of collapse of the axial dipole field that allows a weak, nondipolar field to emerge during the subsequent 10 ka. This onset phase of globally complex field behavior is followed by the final phase of the M-B reversal that is well recorded in the lava flows at Punaruu South, La Palma, and Haleakala (Fig. 3A) during the latter half of MIS 19 (Fig. 3A). Unfortunately, we have been unable to locate or date lava flows that erupted immediately following the final phase of the M-B reversal at 773 ± 2 ka (Fig. 1). However, we note that the normally magnetized Bishop Tuff (*41*, *42*) yields a ^{40}Ar/^{39}Ar age of 764.8 ± 0.3 ka (*37*), and two normally magnetized lava flows at the top of the Punaruu North section, which also have VDM values above 5×10^{22} Am^2, yield ^{40}Ar/^{39}Ar ages of 774.4 ± 8.7 and 772.6 ± 9.3 ka (Figs. 1 and 3C). Thus, on the basis of this sparse volcanic record, we are unable to evaluate the hypothesis that a "rebound" of the magnetic field occurred immediately following the final phase of the M-B reversal (*25*). Unlike other sedimentary records, those at Chiba and Osaka Bay do, perhaps, record a postreversal excursion or rebound between about 766 and 762 ka (Fig. 3B).

The initial lava-defined polarity excursions at ~795 ka coincide with a drop in paleointensity recorded in sediment cores ODP 984 and MD90-961, as well as in the global PISO 1500 stack that is coeval with an enhanced flux of cosmogenic ^{10}Be in the sediment core MD98-2183 (*43*, *44*) and in the Antarctic ice core EDC (*45*, *46*) (Fig. 3C). The subsequent lava-defined excursion at ~784 ka occurs just after the sediment and ice core paleointensity proxies exhibit modest increases. The M-B reversal process itself begins at ~784 ka and continues into the final polarity reversal at 773 ka as the paleointensity proxies each exhibit a decline with the lowest values in the marine sediments occurring at 773 ka, a few thousand years before the maximum ^{10}Be flux in the EDC ice record (Fig. 3C). Compilations of other sediment core records of ^{10}Be variations over the period illustrated in Fig. 3 are mixed, with several cores exhibiting enhanced ^{10}Be correlative with the initial excursions we have found in lavas at 795 ka and others that do not (*43*, *44*). None of these sediment cores carry enhanced ^{10}Be associated with the excursion

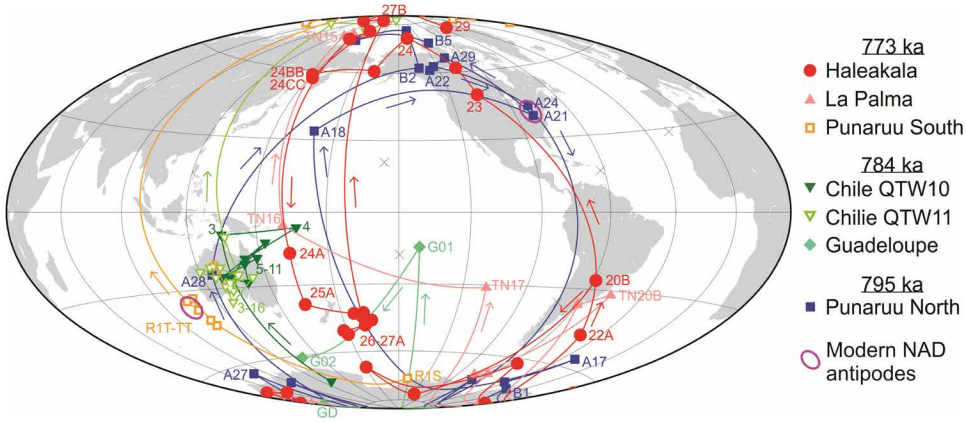

Fig. 4. VGPs from seven lava flow sequences (located at the "×" symbols) that record the M-B reversal process. The historic NAD antipodes (i.e., the average position and antipode of the maximum vertical field of the Australian NAD flux patch between 1590 and 1995 AD) are from (*28*).

captured at 784 ka by the Chilean lavas, perhaps because the deposition rates of these sediments, 2.0 to 4.2 cm/ka, are low (*43*, *44*), and the excursion (as well as the associated weakening of the dipole field) was so short-lived that sediments could not record it [e.g., (*22*, *23*)].

Evolution of geodynamo instability and timing of the M-B reversal

We propose that rather than three successive collapses and regenerations of the dipole field, spanning less than 9 ka, as hypothesized for all polarity reversals of the past 180 million years by Valet *et al.* (*26*), the most recent M-B reversal, for which by far the largest number of high-quality records are available, instead exhibits a more complex evolution of dipole-dominant and nondipole fields spanning at least 22 ka. The tight synchronization of VGPs associated with $^{40}Ar/^{39}Ar$-dated lavas to continuous astronomically dated sediment records shows that dipole field collapse, and thus enhanced production of atmospheric ^{10}Be, occurred initially at ~795 ka, followed by regeneration of a stronger reversed dipole that attenuated cosmogenic nuclide production. The subsequent excursion at ~784 ka may reflect a triggering event within the geodynamo that propelled the dipole field to weaken again. This is recorded not only in lavas but also in sediment cores spanning from the equator to high latitudes (Fig. 3). The final reversal manifests a complex evolution of weak, unstable fields beginning perhaps as early as the triggering excursion at ~784 ka and terminating rapidly—in less than 4000 years—with a full reversal of polarity at 773 ± 2 ka. ^{10}Be production peaks during the final reversal in equatorial sediment and nearly so in high-latitude Antarctic ice. The entirety of this M-B reversal process, now anchored by many $^{40}Ar/^{39}Ar$-dated lavas obtained using an astronomically calibrated FCs standard age (*32*, *36*), spans at least 22 ka and perhaps as long as 30 ka.

Attention has been called to the clustering of transitional VGPs from lavas in both Punaruu Valley sections considered here (*28*, *47*) over eastern North America and near Australia that are nearly coincident with vertical maxima in flux associated with the NAD field of the past 400 years (Fig. 4). This spatial organization of weak nondipolar fields has been interpreted to reflect lower mantle control on fields emerging from the outermost core fluid (*28*, *47*). Our findings here indicate that if this model is correct, then each of the recording sites was affected in a manner that produced similar VGP paths and clustering, suggesting a common guiding physical control on the weak nondipole fields that emerged repeatedly during the >22 ka period that terminated with the M-B reversal at 773 ka (Fig. 4).

The thermochemical numerical dynamo model of (*48*) has produced both simple and complex simulations of reversals. The Case i simulation in (*48*), considered by these authors to be perhaps the most Earth-like of their simulations, features an initial polarity reversal during which field intensity becomes low for about 25 ka, followed by a reversal back to the original polarity and a rather rapid final reversal, with no postreversal rebound. The overall duration from the onset of the precursor to completion of the final reversal is about 50 ka, roughly twice as long as the duration indicated by our observational data (Fig. 3). Thus, the Case i numerical model of (*48*) could provide an excellent starting point from which to design future simulations to explore how lower mantle conditions [e.g., (*28*, *49*)] may have guided the evolution of field direction and intensity that characterizes the M-B reversal.

METHODS

$^{40}Ar/^{39}Ar$ geochronology

Groundmass separates were prepared from lava samples by crushing, sieving to 180 to 250 μm, magnetic sorting, and density separation using methylene iodide. For several of the Haleakala lavas collected in 2015 (samples labeled with H-15- prefix), we isolated the fine (63 to 125 μm) plagioclase comprising the groundmass. However, because experiments on the fine plagioclase produce plateau dates that are less precise than those of the groundmass, we did not pursue additional plagioclase experiments. Purified separates were ultrasonically leached as needed in 1.2 M HCl, rinsed ultrasonically with deionized water, and then hand-picked under a binocular microscope to remove any grains that were made of primarily olivine or clinopyroxene. Samples were irradiated in the CLICIT (cadmium-lined in-core irradiation tube) facility at the Oregon State University TRIGA (Training, Research, Isotopes, General Atomics) reactor. The Alder Creek rhyolite sanidine was used as a neutron fluence monitor. Several recent experiments have obtained essentially identical age data for the Alder Creek sanidine (ACs) standard, when calibrated using the astronomically determined age of 28.201 ± 0.046 Ma (*32*) for the widely used FCs standard (*36*, *50*, *51*). Age determinations here are reported with 2σ analytical uncertainties and are calculated relative to ACs at 1.1864 ± 0.0003 Ma (*37*) using the decay constants of (*52*).

To obtain accurate $^{40}Ar/^{39}Ar$ ages for Pleistocene volcanic rocks, it is essential that the instrument measures Ar isotopes, especially at mass/electron charge (m/e) 36, and not some combination of Ar plus interfering species. The ability of an instrument to resolve interferences is described by the mass resolving power (MRP), which is defined as $m/\Delta m$, where m is the mass of the peak and Δm is the mass difference between 5 and 95% of peak height on the side of the peak (*53*). The MRP of the Nu Instruments Noblesse multicollector mass spectrometer in the WiscAr laboratory at the University of Wisconsin-Madison is ~3000, which is higher than that determined in Noblesse instruments installed before 2015 (*54*) and is also significantly higher than for the single-collector instruments used to obtain data in (*15*) and other previous studies of lavas associated with the M-B reversal. At m/e 36, the MRP of the WiscAr Noblesse allows for $^{36}Ar + H^{35}Cl$ to be partially resolved from the sum peak of $^{36}Ar + H^{35}Cl + {}^{12}C_3$. To avoid any influence of $^{12}C_3$ at m/e 36 and other isobaric interferences at the other masses, measurements are taken on the low mass side of the argon peaks [figure 1 of (*36*)]. Peak position, width, and shape were optimized by first adjusting the source parameters and then changing the voltages of the quadrupole lenses. The same quadrupole settings were used for measurements of blanks, standard gas, and samples.

The Noblesse is attached to a gas extraction system with a Photon Machines Fusions 10.6 60-W CO_2 laser, two SAES GP-50 getters, an ARS cryotrap operating at −125°C, and two gas reservoir/pipette systems. The incremental heating analyses conducted in this study were performed on ~15 to 20 mg of groundmass, which is more than an order of magnitude less material than the ~200 to 450 mg of groundmass used for the incremental heating experiments performed using a resistance furnace by Singer *et al.* (*15*, *31*). Gas released from the samples was cleaned with two SAES GP-50 getters, one at room temperature and one at 450°C, for 3 min followed by exposure to a cryogenic trap for another 90 s. Procedural blanks averaged 8500 counts per second (cps) for ^{40}Ar and ~30 cps for ^{36}Ar, which correspond to ~3 to 4% of the ^{40}Ar and ^{36}Ar signals per heating step.

Our approach to multicollector calibration is described in detail in (*37*) and is similar to (*55*) in that we have developed an in-house standard gas (e.g., cocktail gas) to assess mass discrimination and differences in efficiencies of the IC (ion counter) detectors. Analyses of unknown samples, blanks, and standard minerals are carried out in identical fashion with a routine involving one peak hop. This single routine works for experiments on samples of all ages. During initial measurement of the gas, ^{40}Ar (IC0), ^{39}Ar (IC1), ^{37}Ar (IC2), and ^{36}Ar (IC3) were measured simultaneously, followed by a peak jump of one atomic mass unit where ^{39}Ar (IC0), ^{38}Ar (IC1), and ^{36}Ar (IC2) were measured. This two-step cycle, which takes 20 s, was repeated 15 times. The Faraday detector was not used. During the second step of the cycle (i.e., after the peak hop), the quadrupole focusing lens settings were adjusted to ensure that ^{39}Ar, ^{37}Ar, and ^{36}Ar and measured in the same peak position in both steps.

The peak hop is necessary to obtain $^{40}Ar/^{39}Ar$, $^{36}Ar/^{39}Ar$, and $^{37}Ar/^{39}Ar$ ratios, required to calculate the age of a sample. Accurate and reproducible age determinations using a multicollector mass spectrometer require that mass fractionation effects and the relative efficiencies of the different detectors be well known. This is achieved by repeating a blank-standard-sample routine. Analysis of bracketing standard gas aliquots allows the calculation of correction factors, which incorporate mass discrimination of the source and detector and detector efficiency. Details about how measured ratios are corrected for these factors are in (*37*). Note that for determination of $^{40}Ar/^{39}Ar$, we used an approach that is slightly different from that outlined in (*37*). In that paper, we used the ^{40}Ar and ^{39}Ar measured in the same detector (IC0) and ignored the mass fractionation correction required to convert measured $(^{40}Ar/^{39}Ar)_{IC0}$ to the true $(^{40}Ar/^{39}Ar)_{IC0}$, although this correction is likely minimal. Because we measured $^{40}Ar_{IC0}/^{39}Ar_{IC1}$ in both the standard gas and the sample, we calculated the true $^{40}Ar/^{39}Ar$ in the sample by the same method that the true $^{39}Ar/^{36}Ar$ in the sample was determined.

Correction factors can vary by up to 2 to 6 per mil (‰) over a 24-hour period for groundmass analyses and often <1‰ for sanidine analyses. However, the variation is typically gradual and thus is accurately captured by the standard analyses, which are done every 45 min. The blank-standard-sample routine also allows the evolution of the blanks to be evaluated on the same time scale, which was not possible with single-collector measurements done using a resistance furnace [e.g., (*15*, *32*)], where a small number of temperature-dependent blanks could only be determined before and after an incremental heating experiment (e.g., once every 24 hours). Apart from the dead time correction, which is applied within the Noblesse software, all data reduction (including signal versus time fits) and corrections (e.g., IC dark noise, ^{37}Ar and ^{39}Ar decay, etc.) are carried out offline using an in-house data reduction program, which is a modified version of the ArArCalc freeware program.

Replicate experiments were performed on some samples to improve precision and evaluate accuracy. The age uncertainties reported in Table 1 reflect analytical uncertainties only at the 2σ level (plateau ages include J uncertainty). Our criteria for an acceptable plateau are similar to those of (*56*); a plateau must (i) include three or more consecutive steps that contain ≥50% of the ^{39}Ar released, (ii) have a probability of fit of at least 0.05, and (iii) have no resolvable slope. The MSWDs for the plateau ages in Table 1 are <1 with the exception of those of QTW10-5 (1.13) and QTW11-5 (1.60). We recognize that plateau ages are model dependent and assume that trapped Ar is atmospheric in composition. However, given the uncertainties, all isochrons have y-axis intercepts indistinguishable from the atmospheric $^{40}Ar/^{36}Ar$ value of 298.56 ± 0.31 (*57*). Thus, we infer that the plateau ages reflect the time elapsed since each lava flow cooled through both the Curie temperature and closure to argon diffusion—essentially the age of eruption and lock-in of thermoremanent magnetization. For the samples in which multiple incremental experiments were performed, the isochron age listed in Table 1 was determined using the plateau steps from all of the experiments (i.e., combined isochron) rather than simply calculating a weighted mean of the isochron ages from each experiment of a given sample. Complete Ar isotope data for each sample is provided in the Supplementary Materials.

Paleointensity measurements

Paleointensity measurements were made at Kumamoto University on the samples collected from the lava sequence of Haleakala caldera. One-inch-diameter cores were drilled from the block samples, and the cores were cut into samples of ~22 mm in length. Thirty-nine samples were measured using the Tsunakawa-Shaw paleointensity method (previously called the LTD-DHT Shaw method) using the methods in (*58*).

The experimental conditions are as follows: Alternating field (AF) demagnetization and remanence measurement were made by an automated fluxgate-sensor spinner magnetometer with AF demagnetizer

(Dspin-2, Natsuhara Giken). Progressive AF demagnetization up to 180 mT was applied to the samples. Acquired remanent magnetization (ARM) was given in 50- or 107-μT direct current field with the maximum AF (180 mT) of the AF demagnetizer (see the Supplementary Materials). The ARM was approximately parallel to the natural remanent magnetization or thermal remanent magnetization (TRM). TRMs were imparted to the samples in a vacuum of 10 to 10^2 Pa in a thermal demagnetizing oven (Natsuhara Giken). The hold time at a peak temperature of 610°C in the first heating was 30 min, and in the second heating, it was 40 min. Representative experimental details (figs. S9 to 12) and results (tables S2 to S4) are in the Supplementary Materials.

SUPPLEMENTARY MATERIALS

Supplementary material for this article is available at http://advances.sciencemag.org/cgi/content/full/5/8/eaaw4621/DC1

Fig. S1. Age spectra and isochron diagrams of legacy and new $^{40}Ar/^{39}Ar$ experiments.
Fig. S2. Stratigraphic relationship of 34 lava flows of the lava sequence in the northern wall of Punaruu Valley, Tahiti, that are based on the field observations of Mochizuki *et al.* (*16*).
Fig. S3. AF demagnetization results for flow A27 in Balbas *et al.* [(*36*), supplementary file, p. 29].
Fig. S4. AF demagnetization results for flow site A27 (sample TM23-5-1) in Mochizuki *et al.* (*16*).
Fig. S5. AF demagnetization results for flow site B1 (sample TM32-9-1) in Mochizuki *et al.* (*16*).
Fig. S6. AF demagnetization results for flow site B1 in Balbas *et al.* [(*36*), supplementary documents. p. 32].
Fig. S7. Comparison of WiscAr ages and the plateau ages determined by Balbas *et al.* (*36*) using a multicollector mass spectrometer with Faraday detectors (uncertainties are ±2σ analytical).
Fig. S8. Cumulative probability distribution of $^{40}Ar/^{39}Ar$ dates.
Fig. S9. An example of Tsunakawa-Shaw paleointensity result (sample 85M033-11 from Haleakala flow unit number 53, which is field site 26 in Fig. 1) that meets criteria A.
Fig. S10. An example of Tsunakawa-Shaw paleointensity result (sample H-15-27A-12 from Haleakala flow unit number 59, which is lava site no. 27A in Fig. 1) that meets criteria B.
Fig. S11. Paleointensity estimates from lava flows of the lava sequence in Haleakala caldera on Maui.
Fig. S12. Representative thermomagnetic curves.
Table S1. Typical system blanks for legacy dates and Noblesse multicollector dates.
Table S2. Results of Tsunakawa-Shaw paleointensity experiments on samples from the lava sequence of Haleakala caldera on Maui.
Table S3. Summary of absolute paleointensity estimates from the lava sequence of Haleakala caldera, Maui.
Table S4. Summary of relative paleointensity estimates from the lava sequence of Haleakala caldera, Maui.
Data S1. Table of complete $^{40}Ar/^{39}Ar$ results.
Data S2. Age spectrum and isochron plots of $^{40}Ar/^{39}Ar$ results.

REFERENCES AND NOTES

1. J.-P. Valet, A. Fournier, Deciphering records of geomagnetic reversals. *Rev. Geophys.* **54**, 410–446 (2016).
2. J. E. T. Channell, Complexity in Matuyama–Brunhes polarity transitions from North Atlantic IODP/ODP deep-sea sites. *Earth Planet. Sci. Lett.* **467**, 43–56 (2017).
3. G. A. Glatzmaier, R. S. Coe, Magnetic polarity reversals in the core. *Treatise Geophysics* **8**, 279–295 (2015).
4. N. J. Shackleton, A. Berger, W. R. Peltier, An alternative astronomical calibration of the lower Pleistocene timescale based on ODP Site 677. *Earth Environ. Sci. Trans. R. Soc. Edinb.* **81**, 251–261 (1990).
5. L. Tauxe, T. Herbert, N. J. Shackleton, Y. S. Kok, Astronomical calibration of the Matuyama-Brunhes boundary: Consequences for magnetic remanence acquisition in marine carbonates and the Asian loess sequences. *Earth Planet. Sci. Lett.* **140**, 133–146 (1996).
6. F. C. Bassinot, L. D. Labeyrie, E. Vincent, X. Quidelleur, N. J. Shackleton, Y. Lancelot, The astronomical theory of climate and the age of the Brunhes-Matuyama magnetic reversal. *Earth Planet. Sci. Lett.* **126**, 91–108 (1994).
7. C.-S. Horng, A. P. Roberts, W.-T. Liang, A 2.14-Myr astronomically tuned record of relative geomagnetic paleointensity from the western Philippine Sea. *J. Geophys. Res.* **108**, 2059 (2003).
8. J. E. T. Channell, B. Lehman, The last two geomagnetic polarity reversals recorded in high-deposition-rate sediment drifts. *Nature* **389**, 712–715 (1997).
9. J.-P. Valet, F. Bassinot, A. Bouilloux, D. Bourlès, S. Nomade, V. Guillou, F. Lopes, N. Thouveny, F. Dewilde, Geomagnetic, cosmogenic and climatic changes across the last geomagnetic reversal from Equatorial Indian Ocean sediments. *Earth Planet. Sci. Lett.* **397**, 67–79 (2014).
10. M. Hyodo, D. K. Biswas, T. Noda, N. Tomioka, T. Mishima, C. Itota, H. Sato, Millennial- to submillennial-scale features of the Matuyama-Brunhes geomagnetic polarity transition from Osaka Bay, southwestern Japan. *J. Geophys. Res.* **111**, B02103 (2006).
11. M. Hyodo, I. Kitaba, Timing of the Matuyama–Brunhes geomagnetic reversal: Decoupled thermal maximum and sea-level highstand during Marine Isotope Stage 19. *Quat. Int.* **383**, 136–144 (2015).
12. M. Okada, Y. Suganuma, Y. Haneda, O. Kazaoka, Paleomagnetic direction and paleointensity variations during the Matuyama–Brunhes polarity transition from a marine succession in the Chiba composite section of the Boso Peninsula, central Japan. *Earth Planets Space* **69**, 45 (2017).
13. Y. Suganuma, M. Okada, K. Horie, H. Kaiden, M. Takehara, R. Senda, J.-I. Kimura, K. Kawamura, Y. Haneda, O. Kazaoka, M. J. Head, Age of Matuyama-Brunhes boundary constrained by U-Pb zircon dating of a widespread tephra. *Geology* **43**, 491–494 (2015).
14. R. S. Coe, B. S. Singer, M. S. Pringle, X. Zhao, Matuyama–Brunhes reversal and Kamikatsura event on Maui: Paleomagnetic directions, $^{40}Ar/^{39}$ Ar ages and implications. *Earth Planet. Sci. Lett.* **222**, 667–684 (2004).
15. B. S. Singer, K. A. Hoffman, R. S. Coe, L. L. Brown, B. R. Jicha, M. S. Pringle, A. Chauvin, Structural and temporal requirements for geomagnetic field reversal deduced from lava flows. *Nature* **434**, 633–636 (2005).
16. N. Mochizuki, H. Oda, O. Ishizuka, T. Yamazaki, H. Tsunakawa, Paleointensity variation across the Matuyama-Brunhes polarity transition: Observations from lavas at Punaruu Valley, Tahiti. *J. Geophys. Res.* **116**, B06103 (2011).
17. M. C. Brown, B. R. Jicha, B. S. Singer, J. Shaw, Snapshot of the Matuyama-Brunhes reversal process recorded in $^{40}Ar/^{39}Ar$-dated lavas from Guadeloupe, West Indies. *Geophys. Geochem. Geosyst.* **14**, 4341–4350 (2013).
18. B. S. Singer, A Quaternary geomagnetic instability time scale. *Quat. Geochronol.* **21**, 29–52 (2014).
19. M. J. Head, P. L. Gibbard, Early–Middle Pleistocene transitions: Linking terrestrial and marine realms. *Quat. Int.* **389**, 7–46 (2015).
20. Y. Suganuma, Y. Haneda, K. Kameo, Y. Kubota, H. Hayashi, T. Itaki, M. Okuda, M. J. Head, M. Sugaya, H. Nakazato, A. Igarashi, K. Shikoku, M. Hongo, M. Watanabe, Y. Satoguchi, Y. Takeshita, N. Nishida, K. Izumi, K. Kawamura, M. Kawamata, J. Okuno, T. Yoshida, I. Ogitsu, H. Yabusaki, M. Okada, Paleoclimatic and paleoceanographic records through Marine Isotope Stage 19 at the Chiba composite section, central Japan: A key reference for the Early–Middle Pleistocene Subseries boundary. *Quat. Sci. Rev.* **191**, 406–430 (2018).
21. R. S. Coe, J. M. Glen, The complexity of reversals. Timescales of the Paleomagnetic Field. *Am. Geophys. Union Mon.* **145**, 221–232 (2004).
22. A. P. Roberts, M. Winklhofer, Why are geomagnetic excursions not always recorded in sediments? Constraints from post-depositional remanent magnetization lock-in modelling. *Earth Planet. Sci. Lett.* **227**, 345–359 (2004).
23. J.-P. Valet, L. Meynadier, Q. Simon, N. Thouveny, When and why sediments fail to record the geomagnetic field during polarity reversals. *Earth Planet. Sci. Lett.* **453**, 96–107 (2016).
24. M. E. Evans, A. R. Muxworthy, A re-appraisal of the proposed rapid Matuyama–Brunhes geomagnetic reversal in the Sulmona Basin, Italy. *Geophys. J. Int.* **213**, 1744–1750 (2018).
25. H. Oda, C. Xuan, Deconvolution of continuous paleomagnetic data from pass-through magnetometer: A new algorithm to restore geomagnetic and environmental information based on realistic optimization. *Geochem. Geophys. Geosyst.* **15**, 3907–3924 (2014).
26. J.-P. Valet, A. Founier, E. Courtillot, E. Herrero-Bervera, Dynamical similarity of geomagnetic field reversals. *Nature* **490**, 89–93 (2012).
27. M. N. Gratton, J. Shaw, L. L. Brown, Absolute palaeointensity variation during a precursor to the Matuyama-Brunhes transition recorded in Chilean lavas. *Phys. Earth Planet. In.* **162**, 61–72 (2007).
28. K. A. Hoffman, N. Mochizuki, Evidence of a partitioned dynamo reversal process from paleomagnetic recordings in Tahitian lavas. *Geophys. Res. Lett.* **39**, L06303 (2012).
29. A. Chauvin, P. Roperch, R. A. Duncan, Records of geomagnetic reversals from volcanic islands of French Polynesia: 2. Paleomagnetic study of a flow sequence (1.2–0.6 Ma) from the island of Tahiti and discussion of reversal models. *J. Geophys. Res. Solid Earth* **95**, 2727–2752 (1990).
30. L. L. Brown, B. S. Singer, J. C. Pickens, B. R. Jicha, Paleomagnetic directions and $^{40}Ar/^{39}Ar$ ages from the Tatara-San Pedro volcanic complex, Chilean Andes: Lava record of a Matuyama-Brunhes precursor? *J. Geophys. Res.* **109**, B12101 (2004).
31. B. S. Singer, M. K. Relle, K. A. Hoffman, A. Battle, C. Laj, H. Guillou, J. C. Carracedo, Ar/Ar ages of transitionally magnetized lavas on La Palma, Canary Islands, and the geomagnetic instability timescale. *J. Geophys. Res.* **107**, 2307 (2002).
32. B. S. Singer, M. S. Pringle, Age and duration of the Matuyama-Brunhes geomagnetic polarity reversal from $^{40}Ar^{39}Ar$ incremental heating analyses of lavas. *Earth Planet. Sci. Lett.* **139**, 47–61 (1996).
33. K. F. Kuiper, A. Deino, F. J. Hilgen, W. Krijgsman, P. R. Renne, J. R. Wijbrans, Synchronizing rock clocks of Earth history. *Science* **320**, 500–504 (2008).

34. J. E. T. Channell, D. A. Hodell, B. S. Singer, C. Xuan, Reconciling astrochronological and $^{40}Ar/^{39}Ar$ ages for the Matuyama-Brunhes boundary and late Matuyama Chron. *Geochem. Geophys. Geosyst.* **11**, Q0AA12 (2010).
35. D. F. Mark, P. R. Renne, R. C. Dymock, V. C. Smith, J. I. Simon, L. E. Morgan, R. A. Staff, B. S. Ellis, N. J. G. Pearce, High-precision $^{40}Ar/^{39}Ar$ dating of pleistocene tuffs and temporal anchoring of the Matuyama-Brunhes boundary. *Quat. Geochronol.* **39**, 1–23 (2017).
36. A. M. Balbas, A. A. P. Koppers, P. U. Clark, R. S. Coe, B. T. Reilly, J. S. Stoner, K. Konrad, Millennial-scale instability in the geomagnetic field prior to the Matuyama-Brunhes reversal. *Geochem. Geophys. Geosyst.* **19**, 952–967 (2018).
37. B. R. Jicha, B. S. Singer, A. M. Sobol, Re-evaluation of the ages of $^{40}Ar/^{39}Ar$ sanidine standards and supereruptions in the western U.S. using a Noblesse multi-collector mass spectrometer. *Chem. Geol.* **431**, 54–66 (2016).
38. N. L. Andersen, B. R. Jicha, B. S. Singer, W. Hildreth, Incremental heating of Bishop Tuff sanidine reveals preeruptive radiogenic Ar and rapid remobilization from cold storage. *Proc. Natl. Acad. Sci. U.S.A.* **114**, 12407–12412 (2017).
39. S. Panovska, C. G. Constable, M. Korte, Extending global continuous geomagnetic field reconstructions on timescales beyond human civilization. *Geochem. Geophys. Geosyst.* **19**, 4757–4772 (2018).
40. K. R. Ludwig, Isoplot 3.00: A geochronological toolkit for Microsoft Excel, *Berkeley Geochronology Center Special Publication*, **4**, 70 pp. (2003); http://www.bgc.org/isoplot_etc/isoplot.html.
41. G. B. Dalrymple, A. Cox, R. R. Doell, Potassium-argon age and paleomagnetism of the Bishop Tuff, California. *Geol. Soc. Am. Bull.* **76**, 665–674 (1965).
42. H. C. Palmer, W. D. MacDonald, C. S. Gromme, B. B. Elwood, Magnetic properties and emplacement of the Bishop Tuff, California. *Bull. Volcanol.* **58**, 101–116 (1996).
43. Q. Simon, D. L. Bourlès, N. Thouveny, C.-S. Horng, J.-P. Valet, F. Bassinot, S. Choy, Cosmogenic signature of geomagnetic reversals and excursions from the Réunion event to the Matuyama–Brunhes transition (0.7–2.14 Ma interval). *Earth Planet. Sci. Lett.* **482**, 510–524 (2018).
44. J.-P. Valet, F. Bassinot, Q. Simon, T. Savranskaia, N. Thouveny, D. L. Bourlés, A. Villedieu, Constraining the age of the last geomagnetic reversal from geochemical and magnetic analyses of Atlantic, Indian, and Pacific Ocean sediments. *Earth Planet. Sci. Lett.* **506**, 323–331 (2019).
45. G. M. Raisbeck, F. Yiou, O. Cattani, J. Jouzel, ^{10}Be evidence for the Matuyama–Brunhes geomagnetic reversal in the EPICA Dome C ice core. *Nature* **444**, 82–84 (2006).
46. L. Bazin, A. Landais, B. Lemieux-Dudon, H. Toyé Mahamadou Kele, D. Veres, F. Parrenin, P. Martinerie, C. Ritz, E. Capron, V. Lipenkov, M.-F. Loutre, D. Raynaud, B. Vinther, A. Svensson, S. O. Rasmussen, M. Severi, T. Blunier, M. Leuenberger, H. Fischer, V. Masson-Delmotte, J. Chappellaz, E. Wolff, An optimized multi-proxy, multi-site Antarctic ice and gas orbital chronology (AICC2012): 120–800 ka. *Clim. Past* **9**, 1715–1731 (2013).
47. K. A. Hoffman, B. S. Singer, Magnetic source separation in Earth's outer core. *Science* **321**, 1800 (2008).
48. P. L. Olson, G. A. Glatzmaeir, R. S. Coe, Complex polarity reversals in a geodynamo model. *Earth Planet. Sci. Lett.* **304**, 168–179 (2011).
49. G. A. Glatzmaier, R. S. Coe, L. Hongre, P. H. Roberts, The role of the Earth's mantle in controlling the frequency of geomagnetic reversals. *Nature* **401**, 885–890 (1999).
50. T. A. Rivera, M. Storey, M. D. Schmitz, J. L. Crowley, Age intercalibration of $^{40}Ar/^{39}Ar$ sanidine and chemically distinct U/Pb zircon populations from the Alder Creek Rhyolite Quaternary geochronology standard. *Chem. Geol.* **345**, 87–98 (2013).
51. E. M. Niespolo, D. Rutte, A. L. Deino, P. R. Renne, Intercalibration and age of the Alder Creek sanidine $^{40}Ar/^{39}Ar$ standard. *Quat. Geochronol.* **39**, 205–213 (2017).
52. K. Min, R. Mundil, P. R. Renne, K. R. Ludwig, A test for systematic errors in $^{40}Ar/^{39}Ar$ geochronology through comparison with U/Pb analysis of a 1.1-Ga rhyolite. *Geochim. Cosmochim. Acta* **64**, 73–98 (2000).
53. T. R. Ireland, Invited review article: Recent developments in isotope-ratio mass spectrometry for geochemistry and cosmochemistry. *Rev. Sci. Instrum.* **84**, 011101 (2013).
54. J. M. Saxton, A method for measurement of ^{36}Ar without $H^{35}Cl$ interference. *Chem. Geol.* **409**, 112–117 (2015).
55. M. A. Coble, M. Grove, A. T. Calvert, Calibration of Nu-Instruments Noblesse multicollector mass spectrometers for argon isotopic measurements using a newly developed reference gas. *Chem. Geol.* **290**, 75–87 (2011).
56. W. D. Sharp, P. R. Renne, The $^{40}Ar/^{39}Ar$ dating of core recovered by the Hawaii Scientific Drilling Project (phase 2), Hilo, Hawaii. *Geochem. Geophys. Geosyst.* **6**, Q04G17 (2005).
57. J.-Y. Lee, K. Marti, J. P. Severinghaus, K. Kawamura, H.-S. Yoo, J. B. Lee, J. S. Kim, A redetermination of the isotopic abundances of atmospheric Ar. *Geochim. Cosmochim. Acta* **70**, 4507–4512 (2006).
58. N. Mochizuki, T. Maruuchi, Y. Yamamoto, H. Shibuya, Multi-level consistency tests in paleointensity determinations from the welded tuffs of the Aso pyroclastic-flow deposits. *Phys. Earth Planet. In.* **223**, 40–54 (2013).
59. J. E. T. Channell, J. H. Curtis, B. P. Flower, The Matuyama-Brunhes boundary interval (500-900 ka) in North Atlantic drift sediments. *Geophys. J. Int.* **158**, 489–505 (2004).
60. J. E. T. Channell, D. A. Hodell, C. Xuan, A. Mazaud, J. S. Stoner, Age calibrated relative paleointensity for the last 1.5 Myr at IODP Site U1308 (North Atlantic). *Earth Planet. Sci. Lett.* **274**, 59–71 (2008).
61. J. E. T. Channell, J. D. Wright, A. Mazaud, J. S. Stoner, Age through tandem correlation of Quaternary relative paleointensity (RPI) and oxygen isotope data at IODP Site U1306 (Eirik Drift, SW Greenland). *Quat. Sci. Rev.* **88**, 135–146 (2014).
62. K. Maegakiuchi, M. Hyodo, I. Kitaba, K. Hirose, S. Katoh, H. Sato, Brief sea-level fall event and centennial to millennial sea-level variations during Marine Isotope Stage 19 in Osaka Bay, Japan. *J. Quat. Sci.* **31**, 809–822 (2016).
63. J. E. T. Channell, C. Xuan, D. A. Hodell, Stacking paleointensity and oxygen isotope data for the last 1.5 Myr (PISO-1500). *Earth Planet. Sci. Lett.* **283**, 14–23 (2009).

Acknowledgments: We thank R. Nagata, C. Gilbert, K. Kapahulehua, A. Ho, T. Rodriguez, and T. Duarte for support and participation in field work. L. Brown and A. Chauvin provided samples from Tahiti and Chile. We thank Haleakala National Park superintendent N. Gates for permission to collect materials in 2015. Comments by J. P. Valet and an anonymous reviewer helped improve this manuscript. **Funding:** This study was supported by National Science Foundation grant EAR-1250446. **Author contributions:** B.S.S., R.S.C., B.R.J., and N.M. framed the scope of this study. B.S.S. wrote the initial manuscript, with all authors contributing to its final form. B.S.S., R.S.C., and B.R.J. collected new samples from Haleakala in 2015. The $^{40}Ar/^{39}Ar$ data were measured and assembled by B.R.J. and interpreted by B.R.J. and B.S.S. New paleointensity data were acquired and interpreted by N.M. **Competing interests:** The authors declare that they have no competing interests. **Data and materials availability:** All data needed to evaluate the conclusions in the paper are present in the paper and/or the Supplementary Materials. Additional data related to this paper may be requested from B.S.S.

Submitted 21 December 2018
Accepted 28 June 2019
Published 7 August 2019
10.1126/sciadv.aaw4621

Citation: B. S. Singer, B. R. Jicha, N. Mochizuki, R. S. Coe, Synchronizing volcanic, sedimentary, and ice core records of Earth's last magnetic polarity reversal. *Sci. Adv.* **5**, eaaw4621 (2019).